Hindawi
Mobile Information Systems
Volume 2022, Article ID 1131452, 11 pages
https://doi.org/10.1155/2022/1131452

Research Article

Analysis of Accuracy Rate of Distributed Virtual Reality Face Recognition Based on Personal Intelligent Terminal

Muhua Hu

Mathematics and Physics Department of Chengyi University College, Jimei University, Xiamen, Fujian, China 361021

Correspondence should be addressed to Muhua Hu; humuhua@jmu.edu.cn

Received 30 January 2022; Accepted 25 March 2022; Published 13 May 2022

Academic Editor: Hye-jin Kim

Due to the fact that problem occurs to the traditional algorithm in the internal change process of the sample set, this paper proposes a distributed virtual reality face recognition algorithm based on the personal intelligent terminal. By the utilization of the face image library with multiple description functions through expansion, the pixel intensity of the face image has data information, the original face image can be used to generate a face image with higher intensity pixels, and the mirror image can increase the detailed data information of the image. By effectively combining source domain images with initialization images, a scalable image set can be generated. According to parameter-free modeling, the image can be extended as a personal intelligent terminal. The test sample images of the same category and different source domains can form an image set and finally use the residual discriminant function to complete the face recognition. Finally, the results of the experimental analysis show that the distributed virtual reality face recognition accuracy analysis method proposed in this paper can not only build a face image database with multiple reconstruction functions but also effectively use the correlation within the face samples to improve the accuracy of face recognition and implement face recognition. Compared with other facial recognition algorithms, this algorithm has higher recognition accuracy and faster recognition speed.

1. Introduction

The study of face recognition has a long history. People are usually distinguished based on facial recognition. However, due to the limitation of the comprehensive reasons of theory, practice, and general environment, the problem of face recognition did not attract the attention of academic circles until the middle of the 20th century. In recent years, with the rapid development of society and science technology, computer vision technology, and pattern recognition technology, facial recognition technology has gradually become a hot topic in the field of vision and recognition research [1, 2]. Since the "9.11" incident in the United States, people have put forward higher requirements for information security and concealment, including how to break through the traditional facial inspection and recognition methods. Accurate and fast facial recognition has become the focus of attention. Facial recognition technology is a recognition method based on biological features, which is also a major breakthrough in the history of human vision development. The research field includes image processing, artificial intelligence, and pattern recognition [3, 4]. For fingerprint recognition, voice recognition, and iris recognition and other features, face recognition is more rapid, vivid, and natural, and the face image can be obtained without interfering with the subject's face [5]. For the face of the recognized person, no other restrictions are required, and the face recognition system does not need a dedicated image collection device, so the cost is also low, and the face recognition technology has gradually been favored by people [6, 7]. At present, many researchers in China and other countries have carried out in-depth research on face recognition technology, among which the representative research institutions are the MIT Media Lab and the Artificial Intelligence Laboratory. The Robotics Laboratory of Carnegie Mellon University in the United States, the INR Research Institute in France, and the Beckman Laboratory of the University of Illinois in the United States conducted face tests according to the facial recognition supplier test organized by the National

Bureau of Standards and Technology. Research data on face test shows that the recognition accuracy of face recognition technology in the world has exceeded the average level of human research, and the recognition rate of high-definition and high-quality face images can reach almost 100%. Chinese research on face recognition technology started relatively late, starting in the late 1990s, but with the joint efforts of many research institutions and organizations, remarkable results have been achieved, for example, Chinese Tsinghua University, Peking University, Nanjing University of Science and Technology, and Shanghai Jiaotong University. In the field of facial skin color detection, Tsinghua University has studied the detection method of facial adaptability by improving traditional facial recognition methods and optimizing facial color and features. Shanghai Jiaotong University has completed a multilevel structure face detection and tracking algorithm by using face recognition technologies such as eigenface, template matching, and data information. Despite the complex and changeable environment, the algorithm can accurately identify and track faces with multiple expressions from multiple angles. In terms of the accuracy of face recognition, the face recognition mode proposed by the Automation Laboratory of Harbin Institute of Technology has played a significant role in promoting the further development of intelligent surveillance recognition in China and has made breakthrough progress especially in the research of target tracking, fast face recognition, and detailed analysis [8, 9].

Face recognition is the ability to automatically and accurately detect database information corresponding to faces in complex environments. Usually, due to the difference of the environment, the location of the face cannot be perceived and located in advance. Therefore, it is necessary to judge whether there is a face in the target environment of the study. If there is a face, it is necessary to further determine the specific position corresponding to the face in the collected image. Factors such as light intensity, face size, noise, and changing occlusion may increase the difficulty of face recognition. The goal of face recognition is to accurately detect facial features on the basis of collecting face images and meanwhile divide the face image into two parts: face and nonface, so as to make basic preparations for face recognition. Facial features, also known as facial feature extraction, refer to the use of specialized detection methods to describe the detected facial images and the facial images corresponding to the facial database. Commonly used description methods include geometric feature method, feature extraction method, algebraic feature method, and moiré pattern detection method. Facial recognition actually compares the detected facial image data with the facial images in the precreated database to detect accurate personnel information, mainly how to choose the appropriate facial image matching method and description method. The system architecture of face recognition is closely related to the description method of face images. Usually, the global detection method can be used, or the face matching method based on facial feature description can be used [10, 11].

According to the relevant performance and differential performance existing in the sample that can be effectively used, this paper proposes a distributed virtual reality face recognition algorithm based on the personal intelligent terminal. Distributed virtual reality processing technology can be used to identify medium-intensity pixel data information; the image set with high face image pixels can be used, to build a parameter-free model for the extended image data dictionary and construct sample images of the same category and different source domains. Finally, experiments verify the effectiveness and practicability of the algorithm.

2. Research-Related Algorithms

Definition 1 (distributed virtual reality quantity). The space suspension lattice is used to illustrate the model of the initial suspension lattice of the facial feature data information; it can be defined as a distributed virtual reality quantity, and the expression is

$$S^{(V)} = N_i^l \times N_j^c \times Z, \tag{1}$$

$$V = 2, N \in R, 1 \le i \le \max(N), \tag{2}$$

$$1 \le j \le \max(N), 1 \le Z \le \max\left(N_{x,y}, z\right). \tag{3}$$

In the formula, $S^{(V)}$ represents the distributed virtual reality volume of the face image; the initialization space suspension lattice of the face image is two-dimensional, $V = 2$; $N_{x,y} \cdot z$ represents the coordinates (x, y) corresponding to the distributed virtual reality quantity under the condition of face image stretching; Z represents the corresponding thickness of the distributed virtual reality quantity; N^l, N^c represent the number of rows and columns of the floating lattice of the face image; i and j represent the coordinate coefficient of the lattice D in turn; $N_{x,y} \cdot z$ is expressed as the total length of the z-axis under the three-dimensional coordinate axis after the floating lattice projection of the face image [12].

Then, the minimum distributed VR quantity can be expressed as

$$S^{(2)}\left(d_{i,j,z}\right) = \begin{bmatrix} d_{1,1,z} & d_{1,2,z} & \cdots & d_{1,I,z} \\ d_{2,1,z} & d_{2,2,z} & \cdots & d_{2,I,z} \\ \vdots & \vdots & & \vdots \\ d_{J,1,z} & d_{J,2,z} & \cdots & d_{J,I,z} \end{bmatrix}, \tag{4}$$

$$z = \min\left(N_{x,y} \cdot z\right). \tag{5}$$

Among them, $d_{i,j,z}$ represents the spatial coordinates corresponding to the minimum distributed virtual reality quantity.

Definition 2. The three-dimensional space corresponding to the distributed virtual reality quantity can be expressed as

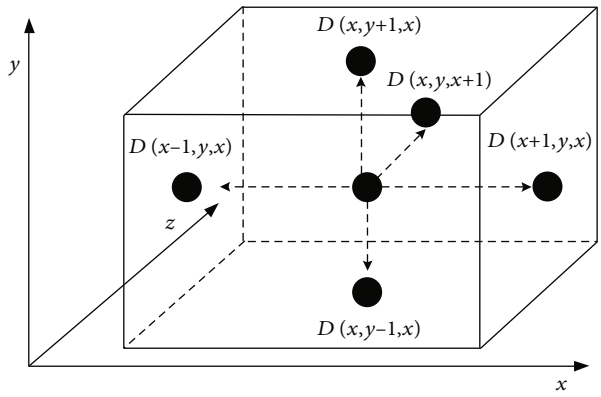

Figure 1: Spatial model of eigenvalues.

the characteristic value of the personal intelligent terminal, and the expression formula is

$$\begin{aligned} \phi_s^{(v)} &= x_N \times y_N \times z_{\mathrm{Dep}}, \\ 1 \le \mathrm{Dep} &\le \max\left(N_{x,y} \cdot z\right), v \equiv 3. \end{aligned} \tag{6}$$

In the formula, s represents the distributed virtual reality quantity, x, y, and z represent the coordinate coefficient of the personal intelligent terminal in turn; Dep represents the depth of the personal intelligent terminal, and the minimum depth represents the minimum value 1 corresponding to the thickness Z of the distributed virtual reality quantity.

The personal intelligent terminal can express it as the n-fold stretch of the z-axis of the minimum distributed virtual reality quantity, and the expression formula is as follows:

$$\phi_s^{(3)}[V(x,y,z)] = \begin{bmatrix} V(0,0,z^+) & V(1,0,z^+) & \cdots & V(x,0,z^+) \\ V(0,1,z^+) & V(1,1,z^+) & \cdots & V(x,1,z^+) \\ \vdots & \vdots & & \vdots \\ V(0,y,z^+) & V(1,y,z^+) & \cdots & V(x,y,z^+) \end{bmatrix}, \tag{7}$$

where

$$V(x,y,z^+) = \begin{bmatrix} \left(x_{\equiv}, y_{\equiv}, z_1^1\right) & \left(x_{\equiv}, y_{\equiv}, z_1^2\right) & \cdots & \left(x_{\equiv}, y_{\equiv}, z_1^n\right) \\ \left(x_{\equiv}, y_{\equiv}, z_2^1\right) & \left(x_{\equiv}, y_{\equiv}, z_2^2\right) & \cdots & \left(x_{\equiv}, y_{\equiv}, z_2^n\right) \\ \vdots & \vdots & \ddots & \vdots \\ \left(x_{\equiv}, y_{\equiv}, z_Z^1\right) & \left(x_{\equiv}, y_{\equiv}, z_Z^2\right) & \cdots & \left(x_{\equiv}, y_{\equiv}, z_Z^n\right) \end{bmatrix}. \tag{8}$$

According to the above expression, $x_{\equiv}, y_{\equiv}$ represents the invariant corresponding to the x- and y-axes; n represents the stretching factor corresponding to the z-axis, which is the depth of the personal intelligent terminal; the value $Z \in [1, \max(N_{x,y} \cdot z)]$; $V(x,y,z)$ represents the corresponding coordinate value of the face image after spatial stretching [10].

Definition 3 (eigenvalues). The spatial radiation vector cluster of the floating point $D^{\phi}_{(x,y,z)}$ corresponding to the personal intelligent terminal and its similar floating point $D^{\phi}_{(x^*,y^*,z^*)}$ can be defined as the eigenvalue and can be expressed as

$$\eta_d^{(v)} = \left(D^{\phi(d)}_{(x,y,z)}, D^{\phi}_{(x^*,y^*,z^*)}\right) = \begin{bmatrix} \left(D^{\phi(d)}_{(x,y,z)}, D^{\phi}_{(x,y,z+1)}\right) & \left(D^{\phi(d)}_{(x,y,z)}, D^{\phi}_{(x,y,z-1)}\right) \\ \left(D^{\phi(d)}_{(x,y,z)}, D^{\phi}_{(x,y+1,z)}\right) & \left(D^{\phi(d)}_{(x,y,z)}, D^{\phi}_{(x,y-1,z)}\right) \\ \left(D^{\phi(d)}_{(x,y,z)}, D^{\phi}_{(x+1,y,z)}\right) & \left(D^{\phi(d)}_{(x,y,z)}, D^{\phi}_{(x-1,y,z)}\right) \end{bmatrix}, \quad d = 1, 2, \cdots, Z. \tag{9}$$

In the formula, d represents the i-th eigenvalue in the personal intelligent terminal, $i \equiv d \in [1, Z]$; the matrix information of the eigenvalues can be expressed with the floating point $D^{\phi}_{(x,y,z)}$ and the suspension points $D^{\phi}_{(x^*,y^*,z^*)}$ corresponding to different directions of up and down, left and right, and front and rear. There are 6 radiation vectors in total. The spatial model of eigenvalues is shown in Figure 1.

Then, the individual radiation vectors can be expressed using the formula

$$\left(D^{\phi(d)}_{(x,y,z)} D^{\phi}_{(x^*,y^*,z^*)}\right) = \begin{bmatrix} \Delta x^* \\ \Delta y^* \\ \Delta z^* \end{bmatrix} = \begin{bmatrix} x'^* - x^* \\ y'^* - y^* \\ z'^* - z^* \end{bmatrix}. \tag{10}$$

x'^*, y'^*, and z'^* in the formula are sequentially expressed as the initialization coordinate coefficient of the radiation vector; Δ indicates the corresponding coordinate error value.

Definition 4 (field space dimension). The three spatial dimensions adopted by the personal intelligent terminal can be expressed as spatial dimensions, and then, the corresponding personal intelligent terminal dimension can be regarded as the first-order dimension [11], which is represented by δ_1^{ε}; the personal intelligent terminal radiation vector cluster, that is, the dimension of the eigenvalue is defined as two-dimensional, represented by δ_2^{ε}; the dimension of a single radiation vector can be defined as three-dimensional, represented by δ_3^{ε}; the expression is as fol-

lows:

$$\delta_3^{\varepsilon} \subset \delta_2^{\varepsilon} \subset \delta_1^{\varepsilon}, \quad \varepsilon \in [0,6],$$

$$\delta_1^{\varepsilon} = \begin{cases} x_1^{\varepsilon}, 0 \le x \le N \\ y_1^{\varepsilon}, 0 \le y \le N \\ z_1^{\varepsilon}, 1 \le z \le N \end{cases} = \begin{cases} \begin{bmatrix} x_2' & x_2'' & x_2''' \\ x''''_2 & x'''''_2 & x''''''_2 \end{bmatrix} \\ \begin{bmatrix} y_2' & y_2'' & y_2''' \\ y''''_2 & y'''''_2 & y''''''_2 \end{bmatrix} \\ \begin{bmatrix} z_2' & z_2'' & z_2''' \\ z''''_2 & z'''''_2 & z''''''_2 \end{bmatrix} \end{cases},$$

$$\delta_2^{\varepsilon} = \begin{cases} x_2^{\varepsilon}, 0 \le \varepsilon \le 6 \Rightarrow \begin{cases} \left\| D_3^{\phi}, x' - D_3^{\phi}.x \right\|_2 \\ \left\| D_3^{\phi}, x'' - D_3^{\phi}.x \right\|_2 \\ \left\| D_3^{\phi}, x''' - D_3^{\phi}.x \right\|_2 \end{cases} \\ y_2^{\varepsilon}, 0 \le \varepsilon \le 6 \Rightarrow \begin{cases} \left\| D_3^{\phi}, y' - D_3^{\phi}.y \right\|_2 \\ \left\| D_3^{\phi}, y'' - D_3^{\phi}.y \right\|_2 \\ \left\| D_3^{\phi}, y''' - D_3^{\phi}.y \right\|_2 \end{cases} \\ z_2^{\varepsilon}, 0 \ge \varepsilon \le 6 \Rightarrow \begin{cases} \left\| D_3^{\phi}, z' - D_3^{\phi}.z \right\|_2 \\ \left\| D_3^{\phi}, z'' - D_3^{\phi}.z \right\|_2 \\ \left\| D_3^{\phi}, z''' - D_3^{\phi}.z \right\|_2 \end{cases} \end{cases} \tag{11}$$

$$\delta_3^{\varepsilon} = \begin{cases} \rho\left(\lambda_x'\sim'''\right) = \begin{cases} \left\| \lambda_x' I - \beta_j \right\| \Rightarrow \rho\left(\lambda_x'\sim'''\right) \\ \left\| \lambda_x'' I - \beta_j \right\| \Rightarrow \rho\left(\lambda_x'\sim'''\right) \\ \left\| \lambda_x''' I - \beta_j \right\| \Rightarrow \rho\left(\lambda_x'\sim'''\right) \end{cases} \\ \rho\left(\lambda_y'\sim'''\right) = \begin{cases} \left\| \lambda_y' I - \beta_j \right\| \Rightarrow \rho\left(\lambda_y'\sim'''\right) \\ \left\| \lambda_y'' I - \beta_j \right\| \Rightarrow \rho\left(\lambda_y'\sim'''\right) \\ \left\| \lambda_y''' I - \beta_j \right\| \Rightarrow \rho\left(\lambda_y'\sim'''\right) \end{cases} \\ \rho\left(\lambda_z'\sim'''\right) = \begin{cases} \left\| \lambda_z' I - \beta_j \right\| \Rightarrow \rho\left(\lambda_z'\sim'''\right) \\ \left\| \lambda_z'' I - \beta_j \right\| \Rightarrow \rho\left(\lambda_z'\sim'''\right) \\ \left\| \lambda_z''' I - \beta_j \right\| \Rightarrow \rho\left(\lambda_z'\sim'''\right) \end{cases} \end{cases}.$$

In the formula, $\rho(\lambda_{x,y,z}\sim''') = \max(|\lambda|)$ represents the spectral radius corresponding to the equation $\|\lambda_z'' I - \beta_j\|$, β_j represents the dimension matrix, I represents the identity matrix, $(x_2'\sim''''''', y_2'\sim''''''', z_2'\sim''''''')$ represents the coordinates of the neighborhood eigenvalues in the second-order dimension in turn, and $(D_3^{\phi}\cdot x'\sim''''''', D_3^{\phi}\cdot y'\sim''''''', D_3^{\phi}\cdot z'\sim''''''')$ represents the offset coordinates corresponding to the eigenvalues of different vectors in the third-order dimension in turn. At this time, the dimension ω of the personal intelligent terminal is expressed as $\omega = \prod_{\substack{1\le i\le 3 \\ 0\le j\le 6 \\ 0\le k\le 3}} \varepsilon_i\varepsilon_j\varepsilon_k$.

Definition 5 (dimension cohesion). If the space dimension corresponding to the quantum space $(\phi_i, i = 1, 2, \cdots, n)$ of distributed virtual reality is represented by $\delta(\phi_i)$, and then, ϕ_i is mainly composed of the eigenvalues $\eta_1 \cdots \eta_m$ and expressed with $\phi_i = \mathrm{coup}(\eta_1 \cdots \eta_m)$; then, for the randomly selected ϕ_i, ϕ_{i+1} in ϕ_i, the following connection relationship of spatial dimensions can exist: $\delta(\phi_i) + \delta(\phi_{i+1}) = \delta(\phi_i + \phi_{i+1}) + \delta(\phi_i \cap \phi_{i+1})$ and finite dimension exist in $\phi_i + \phi_{i+1}$ and $\phi_i \cap \phi_{i+1}$.

Definition 6 (face feature image). Turn the target face image to the personal intelligent terminal, and the obtained three-dimensional face model is regarded as the face feature image Y, which is represented by $Y(\alpha, \beta)$, where α and β represent the depth and dimensional data [11]. Then, the depth data of the facial feature image is represented as follows:

$$\underset{D}{\overset{D}{\alpha}}\left(\mathrm{dep}^{D'}\right) = \begin{bmatrix} \left\| \sum_{S_1 \le D' \le S_2}^{D^1} \mathrm{dep}_{x,y,z}^{D'} \right\|_{\infty} & \cdots & \left\| \sum_{S_{N-1} \le D' \le S_N}^{D^1} \mathrm{dep}_{x,y,z}^{D'} \right\|_{\infty} \\ \vdots & \ddots & \vdots \\ \left\| \sum_{S_1 \le D' \le S_2}^{D^N} \mathrm{dep}_{x,y,z}^{D'} \right\|_{\infty} & \cdots & \left\| \sum_{S_{N-1} \le D' \le S_N}^{D^N} \mathrm{dep}_{x,y,z}^{D'} \right\|_{\infty} \end{bmatrix}. \tag{12}$$

If $T_{i,j,k}$ represents the area corresponding to the eigenvalue dimension in the face feature image space, then the face feature image dimension in this area can be expressed by the following formula:

$$\underset{\delta'}{\overset{\delta^{\varepsilon}}{\beta}}\left(T_{i,j,k}\right) = \begin{bmatrix} \beta_{1,1,k} & \beta_{1,2,k} & \cdots & \beta_{1,N,k} \\ \beta_{2,1,k} & \beta_{2,2,k} & \cdots & \beta_{2,N,k} \\ \vdots & \vdots & \vdots & \vdots \\ \beta_{N,1,k} & \beta_{N,2,k} & \cdots & \beta_{N,N,k} \end{bmatrix}, i \in [0, N],$$
$$j \in [0, N], k \in [1, \max(\mathrm{dep})]. \tag{13}$$

It can be calculated according to the eigenvalues of the facial feature images in the above expressions. The superscript character D of α represents the number of eigenvalues

in the random subspace ($1 \le D \le N$) and the eigenvalue variable of the facial image displayed by the subscript; the mark above β represents the field space dimension, $\delta^{\varepsilon}(0 \le \delta^{\varepsilon} \le 54)$. The subscript represents the dimension scalar of the face image; S_N represents the field scalar of the distributed virtual reality quantity, and S_1 and S_2 represent the metric values of first eigenvalue space and the second eigenvalue space in turn. D^N is the number of eigenvalues in the Nth subspace, and D^1 is the number of eigenvalues in the first subspace.

3. Algorithm Steps

The algorithm steps are as follows.

1. Initialize the original model of distributed virtual reality (see Definition 1).

2. Perform luminance signal detection on the $N \times M$ face image that should be recognized, and calculate the distribution probability of the pixels corresponding to the gray level.

3. Calculate the information entropy value corresponding to each gray level. The information entropy H of the image is

$$H(A) = \sum_{i=1}^{N} p_i \times \log\left(\frac{1}{p_i}\right) = -a_i \sum_{i=1}^{N} p_i \times \log(p_i)s. \quad (14)$$

Here, $H(A)$ represents the information quantity of the random variable A and represents the self-information quantity of the random variable, and in this case, the self-information quantity is 0. $-\log(p_i)a_i p_i = 0 - \log(p_i)$.

4. Calculate the information entropy distribution corresponding to the parallax image, and count the extreme points of the one-dimensional information entropy.

5. Calculate the grayscale corresponding to the case where the maximum value is obtained by the information entropy distribution, and use it as the segmentation threshold for several subregions of the image.

6. The change of gray level in each subregion (increase and decrease of gray level) is positioned from top to bottom using a vector, and the direction and length of the vector represent the direction and width of the change of gray level, respectively [13].

7. Projection of personal intelligent terminal

(1) Compare the gray value of the pixel corresponding to the starting point and end point of each gradient vector with the maximum gray value max τ_j^i, ϖ_j^i, namely, $\varpi_j^i = \tau_j^i / \max(\tau)$, $\varpi_j^i \le 1$.

(2) Each gradient vector is rotated to the personal intelligent terminal model in the three-dimensional direction of the z-axis, and the rotation angle is θ_j^i. $\theta_j^i = \varpi_j^i \times \pi/2 = \pi\tau_j^i/2 \max(\tau), \theta \le \pi/2$.

8. Connect each eigenvalue space formed by each subregion of the projected image to the edge dimension (refer to Definition 5) to form a complete personal intelligent terminal.

9. Identify nose space, eye space, mouth space, and cheek space. Among them, the subspace of the nose is distributed on the outermost part of the personal intelligent terminal, with the high cohesion of the eigenvalues, and the eigenvalues of other subspaces have no interference. The other three spaces can be discriminated according to the corresponding convex and concave features [14].

Figure 2: GT library original image and medium intensity pixel image.

10. Based on the original personal intelligent terminal model, calculate the offset angle of the projected personal intelligent terminal. The position deviation of each subspace is corrected by rotating the corresponding angle of the y-axis of the personal intelligent terminal.

11. Calculate the average density of the eigenvalues of the personal intelligent terminal, count the areas where the eigenvalue density in each subspace is lower than the average density, take the average density as the upper limit of filling, and carry out the filling of eigenvalues (depth and dimension are filled with the average value) and then compensation for small noisy areas of the face.

Suppose m is the maximum value of all pixels and is a regular grayscale image $m = 255$. The method for generating a midintensity pixel image J from the original image I is as follows: I_{ij}

$$J_{ij} = I_{ij} \cdot (m - I_{ij}). \quad (15)$$

J_{ij} represents the intensities of the pixels in the ith row and jth column of the midintensity pixel image J.

From formula (2), it can be obtained: first, if I_{ij} is m or 0, J_{ij} will be 0. Second, if I_{ij} is between 0 and m, then J_{ij} takes the maximum value when it is $m/2$. Third, the closer I_{ij} is to $m/2$, the larger J_{ij} Therefore, in the image of medium-intensity pixels, only the positions of the original image pixels close to the medium pixels are enhanced, and other positions are weakened, which has a significant effect on extracting salient features. The first row of Figure 2 is a partial original image of the GT face database, and the second row is the corresponding midintensity pixel image.

Studies have shown that different pixels play different roles in image classification. Medium-intensity pixels are more stable under changing face images. The original image and the pixel intensity generated image can provide multiple features of the same face image. The fusion of original image, mirror image, and midpixel image constitutes the distributed virtual reality processing technology of this paper,

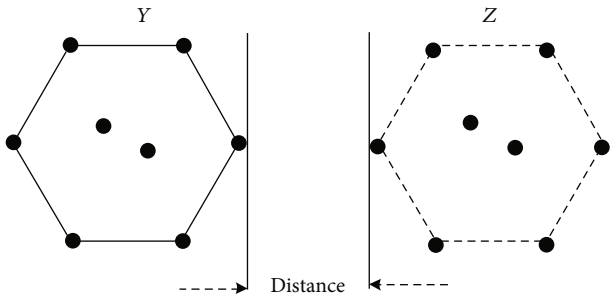

Figure 3: Convex closure of single-set-to-single-set distances.

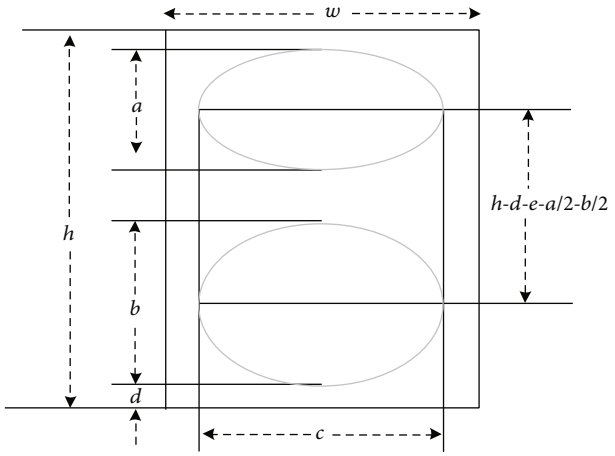

Figure 4: Face mask template structure.

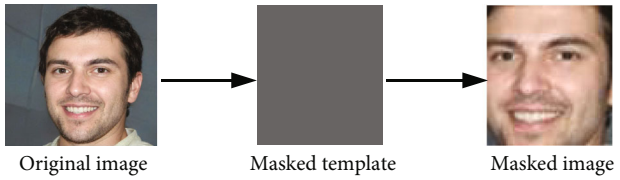

Figure 5: Image masking effect of face recognition.

Figure 6: Partial image of three source domain images of ORL.

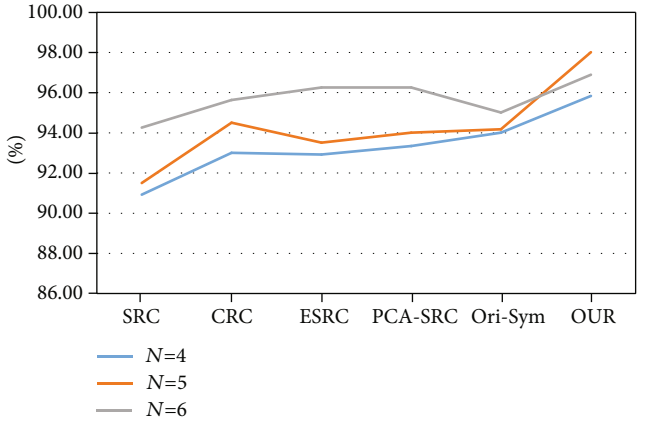

Figure 7: Comparison of positive solution rates of different algorithms in ORL database.

which realizes multiple description of facial images and better completes facial recognition.

Compared to parametric modeling models of image sets, parametric modeling methods have many advantageous properties because no parameter distributions need to be estimated. A simple parameter-free modeling approach is the encapsulation modeling approach that models a set of images as a linear combination of its samples.

Assuming the image set $Y = \{y_1, \cdots, y_i, \cdots, y_{n_a}\}, y_i \in R^d$, the convex closure of the image set Y is defined as $H(Y) = \{\sum a_i y_i\}$. In general, $\sum a_i = 1$ is required and the coefficient a_i is bounded:

$$H(Y) = \left\{ \sum a_i y_i \middle| \sum a_i = 1, \quad 0 \le a_i \le \tau \right\}. \tag{16}$$

Assuming that one image set $Y = \{y_1, \cdots, y_i, \cdots, y_{n_a}\}$ is another image set $Z = \{z_1, \cdots, z_i, \cdots, z_{n_z}\}$, the image set is modeled as a convex closed grouping, and the distance from image set Y to image set Z is defined as

$$\begin{aligned} &\min_{a,b} \quad \left\| \sum a_i y_i - \sum b_j z_j \right\|_2^2 \\ &\text{s.t.} \quad \sum a_i = 1, 0 \le a_i \le \tau \\ &\qquad \sum b_i = 1, 0 \le b_i \le \tau \end{aligned} \tag{17}$$

If the two image sets are disjoint, the single set-to-single set distance of expression (4) is the closest two-point distance of the two convex closed groups, as shown in Figure 3. If each class is viewed as a set of images, the maximum boundary between two classes is the group-to-group distance.

4. Accuracy Analysis of Distributed Virtual Reality Face Recognition

The feature extraction of the face image should be conducted with a corresponding matching method. The statistical method generally adopts the Mahalanobis or Euclidean

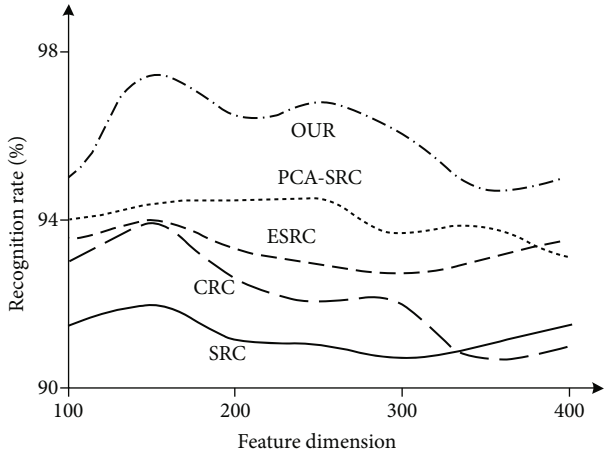

Figure 8: Recognition rates of various algorithms for dimensional changes.

Figure 9: Partial image of GT3 source domain images.

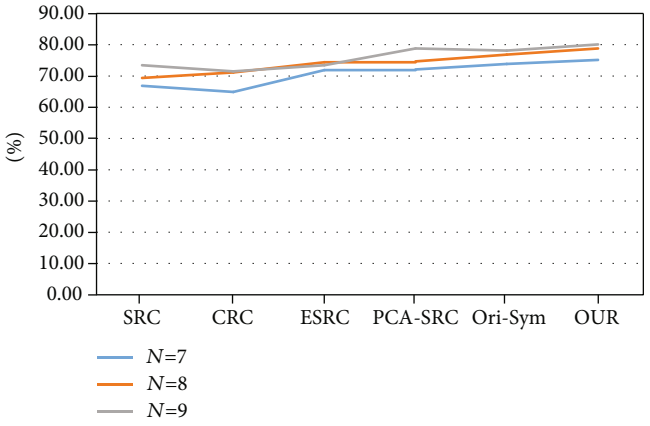

Figure 10: Comparison of the accuracy of different algorithms in the GT database.

distance, and some face recognition systems use the weighted Euclidean distance algorithm. Among them, the template matching method based on the minimum Euclid-

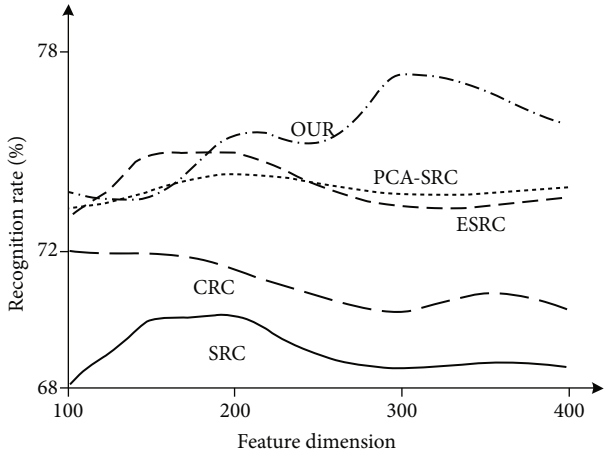

Figure 11: Recognition rates of various algorithms for dimensional changes.

ean distance algorithm is a simple and commonly used method. The basic principle of this method is to assume that the distance modulo value between the face image projected in the feature space and the initial image is the minimum value, and then, the corresponding target can be identified as the original image.

The corresponding operation process is as follows.

(1) Assume a training sample of face images based on the H feature space. Face image test sample. Among them, i represents the number of samples for image training and testing. The KPCA method is used to Mahalanobis process the training samples; to obtain feature vectors, select M eigenvalues from the feature vectors of each group and form the feature space by the feature vectors corresponding to the f eigenvalues. The main eigenvalues of the training samples are all contained in the feature space

(2) Project the value $\varphi(x_i)$ of the training sample x_i in the H space based on the H feature space into the feature space, and then, the mth projection coefficient can be expressed as

$$f_m(x_i) = \left(V_m^T \varphi(x_i)\right) = \sum_{k=1}^{K} \alpha_k^m \left(V_m^T \varphi(x_i)\right). \tag{18}$$

Then, the feature vector $F(x_i) = [f_1(x_i), f_2(x_i), \cdots, f_m(x_i)]^T$ of the training sample x_i is obtained.

(3) Then, project the test sample data $x\{\mathrm{Sd}\}i\{\mathrm{Se}\}$ into the feature space to obtain the corresponding feature vector, which is expressed as

$$F(y_i) = [f_1(y_i), f_2(y_i), \cdots, f_m(y_i)]^T. \tag{19}$$

Figure 12: Partial image of the FERET database set.

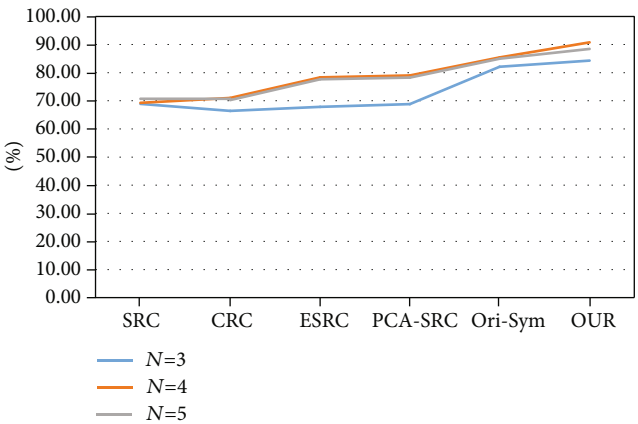

Figure 13: Recognition rates of several methods for FERET face database.

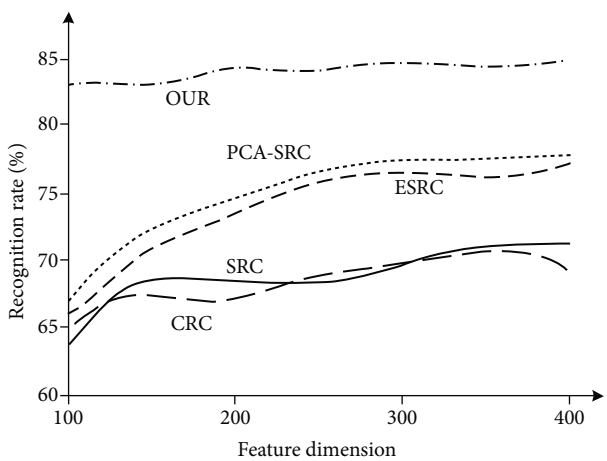

Figure 14: Recognition rates of various algorithms for dimensional changes.

In the formula, $f_m(y_i)$ is the projection coefficient of $\varphi(y_i)$ corresponding to the mth eigenvector.

(4) Minimum Euclidean distance template matching: the Euclidean distance between the feature vectors of image training samples and test samples defined in this paper can be expressed as a measured value close to the two.

$$d(x_i, y_i) = \|F(x_i) - F(y_i)\|^2 = \sum_{m=1}^{M} |f_m(x_i) - f_m(y_i)|^2. \quad (20)$$

According to the above formula, if the minimum value is taken from d, the corresponding template type is the type of the test sample.

This section details the solution of formula (18); although both the $L1$ parameter and the $L2$ parameter can normalize the coefficient vectors a and b, the sparse solution of the $L1$ parameter solution is sparser, so this paper adopts the $L1$ parameter normalization closure to solve the problem.

The $L1$ normalized closing grouping of test set Y is defined as follows:

$$H(Y) = \left\{ \sum a_i y_i \|a\|_{l_1} < \delta \right\} \quad \text{s.t.} \quad \sum a_i = 1 \quad (21)$$

The $L1$ norm regularization closure of distributed virtual reality processing technology is defined as follows:

$$H(X) = \left\{ \sum b_i x_i \|b\|_{l_1} < \delta \right\}. \quad (22)$$

The distance between closure Y and closure X is defined as follows:

$$\min_{a,b} \quad \|Ya - Xb\|_2^2 \quad \text{s.t.} \quad \|a\|_{l_1} < \delta_1, \|b\|_{l_1} < \delta_2, \sum a_i = 1 \quad (23)$$

Equation (23) minimization problem (20) is rewritten in Lagrangian form.

$$\min_{a,b} \quad \|Ya - Xb\|_2^2 + \lambda_1 \|a\|_{l_1} + \lambda_2 \|b\|_{l_1} \quad \text{s.t.} \quad \sum a_i = 1 \quad (24)$$

Here are positive constants for the balance residual and normalization matrix. In the formula $\lambda_1 \lambda_2$, if the test set Y is only one sample and then if $a = 1$, the method simplifies to the SRC process.

Face recognition is easily affected by light intensity, image acquisition angle, and facial expression. In order to improve the effect of face image recognition, it is usually necessary to convert grayscale images from spatial domain representation to frequency domain representation. Among them, Gabor wavelet transform is a commonly used signal and image representation method. In order to avoid storing key features of nonface key features and reduce the feature dimension, this paper extracts the Gabor features of pixels in the corresponding face feature area after the face image is masked by the mask template and excludes the areas

outside the masked area that have little effect on face recognition, which will greatly reduce the dimension of the Gabor feature vector, thereby reducing the space complexity and shortening the processing time of the facial feature extraction algorithm.

The implementation steps of the facial feature extraction algorithm are as follows:

(1) Preprocessing the collected face images

(2) Use the face detection classifier to obtain the face area

(3) The method of human eye detection and pupil positioning is used to lock the position of the human eye and mask the collected face image and correct the facial expression and posture to obtain an effective face area

(4) Gabor feature extraction is performed on the obtained face area, and the image sampling rate is set to 8×8, to obtain LaGrange Gabor features corresponding to valid face regions

The face mask template used in this paper is mainly composed of three parts: ellipse 1, ellipse 2, and rectangle, as shown in Figure 4.

In Figure 4, W represents the width of the face image; h represents the height of the face image; a represents the short axis length of ellipse 1; b represents the short axis length of ellipse 2; assuming that the value of a is 0.5 h, the value of b is 0.85 h, the value of c is 0.75w, the value of d is 0.05 h, and the value of e is 0.1 h. Therefore, the above computable image coordinates are

$$\begin{aligned} &\text{Ellipse 1}: \left[\frac{x-((a/2)+e)}{a/2}\right]^2 + \left[\frac{y-w}{c/2}\right] \le 1.0, \\ &\text{Ellipse 2}: \left[\frac{x-(h-(b/2)-d)}{b/2}\right]^2 + \left[\frac{y-w}{c/2}\right] \le 1.0, \\ &\text{rectangle}\begin{cases} \left(\frac{a}{2}+e\right) \le x \le \left(\frac{h}{2}-\frac{b}{2}-d-e\right), \\ \left(\frac{w}{2}-\frac{c}{2}\right) \le y \le \left(\frac{w}{2}+\frac{c}{2}\right). \end{cases} \end{aligned} \tag{25}$$

The corresponding sample value of any pixel outside the above three valid regions is 0. Therefore, the Gabor wavelet transform algorithm needs to be used only for feature extraction for the pixels in the effective area. For 64×64 face images, the feature dimension of Gabor wavelet transform is 256 using traditional 8×8 acquisition. However, by using the Gabor feature extraction algorithm based on the abovementioned given template parameters and face effective area, the Gabor feature dimension of 1360 can be obtained, and the feature dimension can be reduced by 1200. The reduced image feature dimension is in the nonface key feature regions such as the corresponding hairstyle and shooting background. Figure 5 shows the masking effect of the micro face recognition image.

5. Analysis of Experiment and Results

A series of experiments are performed on the ORL, CMU PIE, GT, and FERET face databases with this method. In addition, based on the classification-based sparse representation algorithm (SRC), the classification-based collaborative representation algorithm (CRC), the sparse representation algorithm (ESRC) combined with the distributed virtual reality processing technology of intraclass variation, the sparse representation algorithm for decentralized virtual reality processing technology combining original images and eigenfaces (PCA-SRC) and decentralized virtual reality processing technology performance algorithm that combines the original image and the mirror image (Ori-Sym) are compared and tested.

The ORL database has 40 people, each with 10 face images. From the knowledge of Section 2.1, the original image and the midpixel image are generated to form the expanded image set. Figure 6 is a partial image of ORL database settings, the first row is the original image, the second row is the mirror image, and the third row is the midpixel image.

In the experiment, $N(=4, 5, 6)$ images are selected for each source image classification to form the distributed virtual reality processing technology, the images in different regions of the same pose form the test set, and the test samples form the image set. The original image size is 56×46. Downsampling is used to downscale the image and provide the recognition rate when the dimension changes.

By combining three source domain training images to construct an extended personal intelligent terminal, an image modeling test closure grouping of the same isotope domain is constructed [15]. Figure 7 compares the classification-based sparse representation algorithm (SRC), the classification-based collaborative representation algorithm (CRC), and the sparse representation algorithm of the intraclass variation joint distribution virtual reality processing technology (ESRC), sparse representation algorithm of decentralized virtual reality processing technology (PCA-SRC) that combines the original image and feature face, and the decentralized virtual reality processing technology representation algorithm (Ori-Sym) that combines the original image and the mirror image, and the accurate recognition rate of different training samples of this method.

Experiments are carried out at different dimensions of the image, using the classification-based sparse representation algorithm (SRC), the classification-based collaborative representation algorithm (CRC), and the sparse representation algorithm with intraclass variation joint distribution virtual reality processing technology (ESRC); under the dimensional change of this method, the sparse representation algorithm (PCA-SRC) of the decentralized virtual reality processing technology that combines the original image and the eigenface is compared [16, 17]. Figure 8 shows the recognition rate curve of the various algorithms in different dimensions of the image. As can be seen from Figure 8, the recognition rate of this method is higher than that of other algorithms.

The GT (Georgia Tech Face Database) database is 50 people, and each person has 15 face images. An extended dataset is formed by generating original images and midpixel images from the knowledge of Section 2.1. Figure 9 is a partial image of the GT database, the first row is the original image, the second row is the mirror image, and the third row is the midintensity pixel image.

For each source image classification, $N(=7, 8, 9)$ images are selected to constitute the distributed virtual reality processing technology, the images of the same pose and heterogeneous regions constitute the test set, and the test samples constitute the image set. The whole image is processed in grayscale, and the image is processed by dimensionality reduction to provide the recognition rate when the dimension changes.

By combining training images of three source domains, construct an extended personal intelligent terminal and establish an image modeling test closure grouping of the same isotope domain. Figure 10 shows the accurate recognition rate of SRC, CRC, ESRC, PCA-SRC, and Ori-Sym and the number of different training samples of this method.

We conduct experiments on the effect of dimensional changes on the algorithm and compare SRC, CRC, ESRC, and PCA-SRC with this method in dimension variation. Figure 11 is the recognition rate curve of various algorithms when the dimension changes.

The FERET face database contains 200 people, and each person contains 7 face images. $N(=3, 4, 5)$ images were selected for each source image classification to constitute the distributed virtual reality processing technology, and the images of the isotopic heterologous regions constituted the test image set. The original image size of the database is 80×80. The image is dimensionally downsampled using downsampling, and the recognition rate is provided when the dimension changes.

The knowledge of generating raw images as mirror images and midpixel images forms the dataset. Figure 12 is a partial image of the FERET database set, the first row is the original image, the second row is the mirror image, and the third row is the midintensity pixel image.

Figure 13 compares the accurate recognition rates of SRC, CRC, ESRC, PCA-SRC, and Ori-Sym and the number of training samples of this method, respectively.

In order to further verify the performance of this algorithm, SRC, CRC, ESRC, and PCA-SRC are compared with this method for dimensional changes. Figure 14 is the change curve of the recognition rate of each algorithm in different dimensions.

6. Conclusion

The rapid development of computer vision technology has promoted the continuous progress of face recognition technology. Face recognition using human intelligent terminals has been widely used in all walks of life due to its high recognition rate and fast speed. This paper optimizes and improves the traditional face feature detection method based on Gabon filter in the face feature extraction process by using the personal intelligent terminal to extract the eigenvalues in the face image. In this paper, we propose to apply the Gabon feature extraction method to valid regions of the image face. This method creates a mask model for the face image by using a mask template, obtains an effective face recognition area, extracts the features of the image pixel Gabon in the obtained effective face recognition area, and discards worthless pixel areas outside the valid recognition area. The facial recognition system reduces the time required for image recognition and reduces the space complexity. Finally, the experimental test shows that the face recognition method designed and implemented in this paper can accurately recognize the face image, operate smoothly, and achieve the expected target effect. Because the algorithm proposed in this paper does not have significant effect on the face image with changes in light intensity and posture during the process of extracting the main features of the image, the complex in-depth study of the ambient light and obvious face image recognition with obvious different postures under the personal intelligent terminal is conducted subsequently.

Data Availability

The data used to support the findings of this study are available from the corresponding author upon request.

Conflicts of Interest

The author declares no conflicts of interest.

Acknowledgments

This research study is sponsored by the Educational Research Project for Young and Middle-Aged Teachers in Fujian Province in 2019 (Science and Technology). The name of the project is Face Recognition Dormitory Management System Based on Deep Learning. The project number is JAT191167. We thank the project for supporting this article.

References

[1] P. J. Phillips, A. N. Yates, Y. Hu et al., "Face recognition accuracy of forensic examiners, superrecognizers, and face recognition algorithms," *Proceedings of the National Academy of Sciences*, vol. 115, no. 11, pp. 107–112, 2018.

[2] S. D. Ganesan and M. Mohammed, "A hybrid face image contrast enhancement technique for improved face recognition accuracy," *International Journal of Intelligent Engineering and Systems*, vol. 10, no. 6, pp. 106–115, 2017.

[3] D. S. Trigueros, M. Li, and M. Hartnett, "Generating photorealistic training data to improve face recognition accuracy," *Neural Networks*, vol. 134, no. 9, pp. 86–94, 2021.

[4] V. Albiero, K. Zhang, M. C. King, and K. W. Bowyer, "Gendered differences in face recognition accuracy explained by hairstyles, makeup, and facial morphology," *IEEE Transactions on Information Forensics and Security*, vol. 17, pp. 127–137, 2021.

[5] N. Medić, Z. Anišić, B. Lalić, U. Marjanović, and M. Brezocnik, "Hybrid fuzzy multi-attribute decision making model for evaluation of advanced digital technologies in manufacturing: Industry 4.0 perspective," *Advances in Production Engineering & Management*, vol. 14, no. 4, pp. 483–493, 2019.

[6] C. K. Tran, C. D. Tseng, C. S. Shieh, and T. F. Lee, "Face recognition under varying illumination conditions: improving the recognition accuracy for local ternary patterns based on illumination normalization methods and singular value decomposition," *Journal of Information Hiding & Multimedia Signal Processing*, vol. 8, no. 4, pp. 957–966, 2017.

[7] L. G. Vu, A. Alsadoon, P. W. C. Prasad, and A. M. S. Rahma, "Improving accuracy in face recognition proposal to create a hybrid photo indexing algorithm, consisting of principal component analysis and a triangular algorithm (pcaata)," *International Journal of Pattern Recognition & Artificial Intelligence*, vol. 31, no. 1, article 1756001, 2017.

[8] X. Chu, L. Jian, and Z. Houcan, "Study on the accuracy of metacognitive monitoring based on the new task of face recognition," *Psychological Exploration*, vol. 12, no. 5, pp. 97–116, 2017.

[9] S. S. Danraka, S. M. Yahaya, A. D. Usman, A. Umar, and A. M. Abubakar, "Discrete firefly algorithm based feature selection scheme for improved face recognition," *Computing and Information Systems*, vol. 23, no. 2, pp. 23–34, 2019.

[10] L. Feng, Z. Qijun, L. Xiaoming, and Z. Dan, "Joint face alignment and 3d face reconstruction with application to face recognition," *IEEE Transactions on Pattern Analysis and Machine Intelligence*, vol. 8, no. 4, pp. 59–72, 2020.

[11] K. Delac, M. Grgic, and S. Grgic, "Image compression effects in face recognition systems," *Marine Policy*, vol. 34, no. 3, pp. 690–698, 2017.

[12] M. Alberto, R. Iga, A. Luis, and C. Andrés, "Influence of cross-ethnic social experience on face recognition accuracy and the visual perceptual strategies involved," *International Journal of Intercultural Relations*, vol. 65, pp. 42–50, 2018.

[13] J. H. Grabman and C. S. Dodson, "Stark individual differences: face recognition ability influences the relationship between confidence and accuracy in a recognition test of game of thrones actors," *Journal of Applied Research in Memory and Cognition*, vol. 9, no. 2, pp. 254–269, 2020.

[14] S. D. Davis, D. J. Peterson, K. T. Wissman, and W. A. Slater, "Physiological stress and face recognition: differential effects of stress on accuracy and the confidence–accuracy relationship," *Journal of Applied Research in Memory and Cognition*, vol. 8, no. 3, pp. 367–375, 2019.

[15] R. Ojstersek, D. Lalic, and B. Buchmeister, "A new method for mathematical and simulation modelling interactivity: a case study in flexible job shop scheduling," *Advances in Production Engineering & Management*, vol. 14, no. 4, pp. 435–448, 2019.

[16] J. G. Cavazos, P. J. Phillips, C. D. Castillo, and A. J. O'Toole, "Accuracy comparison across face recognition algorithms: where are we on measuring race bias?," *IEEE Transactions on Biometrics Behavior and Identity Science*, vol. 3, no. 1, pp. 101–111, 2021.

[17] S. Sutarti, A. T. Putra, and E. Sugiharti, "Comparison of pca and 2dpca accuracy with k-nearest neighbor classification in face image recognition," *Scientific Journal of Informatics*, vol. 6, no. 1, pp. 64–72, 2019.